

Absolute Airborne Thermal SST Measurements and Satellite Data Analysis from the  
Deepwater Horizon Oil Spill

W.S.Good<sup>1</sup>, R. Warden<sup>1</sup>, P.F. Kaptchen<sup>1</sup>, T. Finch<sup>1</sup>, W.J. Emery<sup>2</sup>, A. Giacomini<sup>3</sup>

1. Ball Aerospace, 1600 Commerce St., Boulder, CO, 80301
2. Aerospace Eng. Sci. Dept., Univ of Colorado, Boulder, CO, 80303
3. Informatics Department, Tor Vergata University, Rome, Italy

**Abstract:**

Rapid assessment and continuous monitoring was critical to addressing the changing conditions in response to the Deepwater Horizon Oil Spill. Airborne, satellite, ship-borne, and underwater sensors were all used with data being assimilated as actionable reports. To assist with the recovery effort and evaluate the utility of new sensors for oil spill response, Ball Aerospace sent a team of scientists and engineers to the Gulf in July 2010. The team deployed on a Twin Otter aircraft with a suite of sensors including a thermal imaging radiometer, ultra-violet to visible hyperspectral imaging radiometer, and a visible high dynamic range context imager. All three sensors were operated at the same time with overlapping fields of view to assist with targeting and characterization of the oil. Data was also gathered from satellite synthetic aperture radar (SAR) and optical sensors during the same time and analyzed to determine additional capabilities from these sources. The ultra-violet and thermal imaging capabilities demonstrated were unique when compared with other airborne sensors flown over the spill. In the optical spectral range, imagery from the WorldView 2 satellite operated by DigitalGlobe was utilized while SAR imagery was collected by the TerraSAR-X, COSMOSkyMed (also X-band) and the ENVISAT Advanced SAR (ASAR, C-band). This combination of optical and radar imagery proved very useful in being able to map oil features on the surface of the Gulf of Mexico. Results of the thermal measurements are presented along with a discussion of the other sensor data used to further characterize the spill.

## 1. Background

Oil spill monitoring and characterization requires a suite of sensors with varying capabilities. Several sources [*Fingas and Brown, 2000; Jha et al., 2008*] have reviewed the strengths and weaknesses of different sensors ranging from ultraviolet and visible sensors to passive microwave and SAR. SAR systems have been shown to be very effective at locating and mapping oil spills with the capabilities to see through clouds, but if the wind in the area is too light or too strong, the signal can be corrupted. SAR is also generally unable to detect oil thickness parameters. Visible and UV sensors are capable of detecting oil thickness as well as location but are blocked completely by clouds or sun-glint conditions. Thermal sensors also can offer advantages for detecting oil location and thickness while operating at night as well as during the day. As with UV-Vis sensors though, thermal sensors cannot measure through clouds.

SAR is well known for being able to sense oil on the sea surface due to the damping effect of the oil on the capillary waves at the ocean's surface which reduces the radar backscatter [*Gade et al., 1998*]. Thus, oil features appear as "dark" relative to the brighter SAR sea clutter due to the presence of the wind driven capillary waves. This damping effect is most effective at shorter radar wavelengths such as C or X band and the oil versus open water contrast ratio increases with increasing frequency [*Gade et al., 1998; Wismann et al., 1993*]. As a result we have only considered C and X band SAR data.

The advantage in using SAR imagery to sense oil slicks is that it is all-weather and functions at nighttime as well as during the day. This is very different from the optical

imagery, which requires daytime illumination and low cloud cover to be able to view the sea surface. In this way these different satellite data sets prove to be very complimentary. The visible-near infrared (VIS-NIR) data will provide high spatial resolution multi-channel information while the SAR will supply all-weather and day/night sensing capability. As the sensing capabilities are slightly different it can be expected that each data source will give a slightly different form of the oil slick.

The possibility of detecting and mapping oil spills in optical satellite images has been demonstrated by *Hu et al.*, [2000]. Multi-spectral optical sensors have the potential for detailed identification of the oil spill type (light or crude oil) and estimations of their abundance/thickness. In addition, since oil spills have a higher thermal conductivity they become heated faster from above and become warmer than the surrounding seawater during the daytime making them distinguishable in infrared satellite imagery. At night the oil loses heat faster than the seawater becoming cooler than its surroundings [*Tseng and Chiu*, 1994].

Mapping oil slicks with optical imagery is more difficult than with SAR due to the problems of day only sensing and then only under ideal weather conditions (low cloud cover). The need for atmospheric corrections over and above the cloud filtering also complicates the retrieval of oil slick conditions with optical imagery. Still there is the potential for estimating the thickness of the oil slick that is not possible with a single band SAR image.

One important aspect of optical remote sensing of oil on the ocean is the accurate calibration of the optical sensor. This calibration step converts the raw reflectances into radiance values that represent the radiation upwelling from the ocean's surface. In our study we used spectral radiance to take advantage of the multispectral images collected by WV2. These spectral radiances have the units of  $Wsr^{-1}m^{-3}$ .

Due to the varied capabilities of the sensors, it is recommended to employ a suite of sensors for an oil spill region [Jha *et al.*, 2008]. Both satellite and airborne sensors are often used. Satellites provide broad coverage while airborne assets provide high temporal and spatial resolution. It is a combination of the strengths of all these systems that provides the full picture in the response to an oil spill.

## **2. The Flight System**

Ball Aerospace deployed a suite of instruments on a Twin Otter aircraft contracted from Twin Otter International over the Gulf oil spill on July 9-10, 2010. The instruments, shown mounted on the plane in Figure 1, collected simultaneous data during each flight. Details regarding spectral range, fields of view, and other key parameters are shown in Table 1 with a more detailed discussion of each instrument in the following sections. Footprint and swath width parameters are listed for the actual flight altitude of 1,070 meters (3,500 ft) MSL.

The Ball Experimental Sea Surface Temperature (BESST) radiometer was designed and built by Ball Aerospace to provide a well calibrated measure of sea surface temperature

(SST) from an airborne platform. The Ball sensor suite provided a complementary and spectrally unique data set to other sensors flown over the region.

### **2.1 Ball Experimental Sea Surface Temperature (BESST) Radiometer**

The BESST is a low-mass, low-power SST sensor designed for rapid airborne deployment and shown in Figure 2. It uses a 324 x 256 array of VO<sub>x</sub> microbolometers to sense infrared radiation from the ocean 'skin' temperature. The microbolometers eliminate the need for power hungry cryocoolers or cryogenic fluids which greatly simplifies flight requirements for operation. The measured noise equivalent change in temperature (NEDT) of the BESST instrument is 0.1 K providing the resolution required to distinguish oil and perform remote scientific thermal analyses. Laboratory calibrations of BESST indicate an absolute temperature accuracy of 0.3 K for individual pixels. The key to maintaining this accuracy in the field with varying instrument conditions is on-board calibration blackbodies. During operation, the instrument periodically views the onboard blackbodies to adjust for temperature changes within the instrument and detector.

BESST includes three thermal bands covering the 8-13 um range of the sensor. There is a broadband 8-13 micron window for maximum signal to noise measurements and two narrow 1.0 micron wide bands centered at 10.5 and 11.5 microns. The narrow band filters are used to characterize the atmospheric transmission of the thermal signal due to water vapor in between the sensor and the surface of the water.

## **2.2 GLobal IMager for Marine Ecosystem Research (GLIMMER)**

GLIMMER is a compact, UV-enhanced, hyperspectral ocean color imager also developed by Ball Aerospace. It uses diffraction gratings for dispersion and covers the 350 nm to 700 nm spectral range. GLIMMER, shown in Figure 1, is a pushbroom imager providing swaths of spectral data that are accumulated into spatial images as the plane flies. The instrument includes a unique time-domain polarization scrambler that reduces systematic errors associated with ocean scene polarization variability. In addition to the data shown, results from the flight measurements with GLIMMER will be presented at the SPIE Optics & Photonics Conference in August 2011.

## **2.3 Low Light Imager (LLI)**

LLI is a visible broadband context imager that operates over a dynamic range greater than seven orders of magnitude with  $\text{SNR} > 10$  at the low end of the dynamic range,  $2.85 \times 10^{-9} \text{ W/cm}^2\text{-sr}$  [Osterman *et al.*, 2010]. This performance enables imaging in broad daylight as well as scenes illuminated only by a quarter moon. It is capable of saturation-free imaging of scenes spanning the earth's terminator. The LLI was used to provide context imagery of the oil region and to help discern oil sheen areas that are not detectable by thermal IR imagery.

## **2.4 Multi-spectral Satellite Imagery**

The optical imagery used in this study was high-resolution imagery from DigitalGlobe's WorldView 2 (WV2) satellite. It has a 50 cm resolution panchromatic band as well as

1.8 m resolution 8 spectral channels from 450 nm visible to 1050 nm in the near infrared (Figure 3). Geolocation accuracy was close to the 1.8 m spatial resolution.

### **3. Results**

Measurements in the UV-Vis and thermal wavelength ranges were collected from 1,070 meters above the surface of the Gulf. The Twin Otter airplane was traveling at 50 m/s during the collections to maximize the spatial resolution in the measurements. Baselines in open water were collected prior to entering oily water. The flight lines were flown from the coast of Mississippi over the spill region and back.

#### **3.1 BESST Thermal Radiometer**

##### **Thermal detection of oil on the water surface**

The absolute calibration achieved with the on-board blackbodies for the BESST instrument is key to the detection and distinction of oil on the surface of water. Oil can show up as cooler or warmer than the surrounding water based on the thickness [Fingas and Brown, 2000] and time of day. The measured temperature difference is caused by solar heating of the skin layer during the day. The thermal parameters of the oil relative to the water create a measureable thermal signature. Oil has a lower specific heat than water and thus will heat up faster than water with the same incident solar energy. This also leads to a “cool” signature for oil at night due to the oil giving off thermal energy faster than the surrounding water. Regions of thick oil are where skimmers can be most effective at removing oil from the water and hence are important to identify and report rapidly to responders. Thick oil areas (>500 microns), with higher specific heat than the water, provide warmer temperature measurements than found in the surrounding water



[*Tseng and Chiu, 1993*]. An example image in thick oil is shown in Figure 4(b) with temperatures measured up to 34 degrees C. Also included is an image of clear water showing the skin temperature near the Deepwater Horizon oil spill region which on average was close to 27 degrees C. The thermal imager displayed its ability to detect these regions for future spill response efforts.

Thinner oil regions (0 – 150 microns) are difficult to detect with thermal measurements. Thicknesses of 50-300 microns can appear cooler than the surrounding water potentially due to interference effects of the reflected thermal radiation by the thin layer of oil and a slightly lower emissivity [*Fingas and Brown, 2000; Tseng and Chiu, 1993*]. Very thin (1-5 micron) oil areas require the use of a different type of sensor such as an ultraviolet sensitive instrument.

### **Mapping out oil regions**

Near real-time tracking of oil spill regions is critical to provide an effective response. Daily variation in the spill location due to weather, currents, and mitigation efforts can be quite significant as shown in the example in Figure 5. Ball's flights on July 9<sup>th</sup> and 10<sup>th</sup> were both over the Deepwater Horizon Surface site. Due to slightly different flight lines and the changing oil location, oil was only detected with the thermal sensor on July 9<sup>th</sup> in the white region shown in Figure 5 (a). For the flight on July 10<sup>th</sup>, the oil had moved significantly to the South and East and was not detected during the flight by the thermal sensor, Figure 5 (b). The white polygons are an approximate outline of the measured oil location on the Environmental Response Management Application (ERMA) website

(<http://www.geoplatform.gov/gulfresponse>) during the two days. The measurements with BESST were consistent with the composite locations generated by combining satellite and airborne measurements. The heat signature in the white region confirmed thick oil on the water similar to the image of Figure 4(b) on July 9<sup>th</sup> and no oil measured on July 10<sup>th</sup> consistent with the map showing the flight line staying out of the oil region in Figure 5(b).

### **3.2 GLIMMER – UV-VIS**

An important addition to the sensor suite was the UV channel of the GLIMMER spectrometer. Variations in intensity of the reflected solar signal from the water and oil on the surface can assist with determination of oil position for very thin oil. Oil has a higher reflectivity than water in the UV, so it will appear brighter in UV images. Oil thicknesses of less than 1 micron up to 10 microns can be detected with a UV sensor [*Jha et al.*, 2008]. GLIMMER's narrow spectral sampling in the UV allows detection of intensity variations to be visible even in bands of 2 nm spacing as shown in Figure 6. Band averaging and a band ratio algorithm have the potential to extract more information about the constituent type and characteristics of the oil. These studies are ongoing.

### **3.3 Low Light Imager (LLI)**

Context imagery is important to help characterize the scene observed by thermal and hyperspectral sensors. A broadband visible image from LLI over an oily water region is shown in Figure 7 along with the flight transect and location of the image relative to the Deepwater Horizon Platform.

### **3.4 SAR Sensing of Oil Features**

To give some background for the detailed mapping of the satellite sensed oil slick features we present here in Figure 8 a map put out by Mitch Roffer and the Univ of South Florida based on Advanced Very High Resolution Radiometer (AVHRR) and Landsat satellite imagery that shows the general area covered by the oil slicks in the period between May and July, 2010.

#### **TerraSAR-X Oil Features**

The TerraSAR-X images in Figure 9 from July 5, 2010 show many of the different expressions of oil on the sea surface. Located near the Deepwater Horizon site this image also exhibits the tracks of a number of ships working in the area.

To demonstrate the ability of SAR imagery to discriminate between open water and oil covered water we selected a number of sites (boxes) in Figure 9 and analyzed the oil and water contents of each box. The backscatter components for these various areas are plotted in Figure 10, which very clearly demonstrates how oil suppresses the backscatter from the sea surface.

On July 6, 2010 TerraSAR-X captured the signature of a cold eddy that could also be clearly located in coincident satellite altimetry as shown in Figure 11. The cold eddy managed to trap oil at the surface which produced the low backscatter signature of the eddy in the SAR imagery of Figure 13.

## **Cosmo-SkyMed Imagery**

We also analyzed data from the Cosmo SkyMed (CSK) X-band SAR satellites (provided by the Italian Space Agency to Tor Vergata Univ.). One unique aspect of this data is that this sensor is dual polarized making it possible to examine both VV and HH polarized SAR images of the Gulf of Mexico during the Deepwater Horizon event. A pair of images from April 25, 2010 is presented here in Figure 12.

It is easy to recognize that the contrast in the two images between dark and bright spots is much more distinct in the VV polarization than in the HH image. This was also very clear in the analysis of the radiance values in the various sites selected. The difference in the VV image between the dark oil regions and the lighter open-water areas was about 10 dB, which is about the same as was found for the TerraSAR-X images.

It is also larger than the differences found by analyzing C-band SAR images from ENVISAT's ASAR instrument. This greater sensitivity of the X-band SAR to these polarization differences is further evidence that X-band is the best SAR frequency for the analysis of oil on the surface of the ocean. This comparison between C-band and X-band sensing of an oil slick is best demonstrated in Figure 13 which shows part of Figure 9 repeated with a coincident ASAR image with similar labels. The lower resolution of the C-band SAR is readily apparent as are the much fuzzier boundaries between oil and open-water.

### **3.5 Oil thickness analysis using WorldView-2**

To develop a good understanding of the optical patterns in oil covered areas we used cases where we had coincident SAR and optical imagery. In this way we could use the SAR imagery to clearly define the oil-covered area and see how the VIS-NIR data differed in this area from the surroundings.

Two examples are given in Figure 14, which show WorldView 2 spectral profiles for two different portions of SAR images containing oil. On the left are shown reflectances for an oil-covered region. The center represents the border region between oil and open-water. On the right are spectral profiles for open water.

The difference between open-water and oil covered water is very clear particularly in the middle wavelengths which show much larger values for open-water than they do for oil. The border regions are clearly dominated by the oil present in that their spectral signatures are very similar to those for oil-covered regions. Thus, it is the mid-range visible wavelengths that most clearly depict the difference between oil-covered and open-water conditions. Here the spectral energy is higher for these mid-range wavelengths.

These spectral differences can be exploited to estimate the thickness of the oil slick being sensed. First, we recognize that the spectral radiance decreases from a maximum at about 0.4  $\mu\text{m}$  with increasing wavelength to about 0.0 above 0.9  $\mu\text{m}$ . Second, the trends for all wavelengths going from the center of the oil spill to its edge are similar except for channel 5 ( $\sim 0.6 \mu\text{m}$ ). Channel 5 data changes as you approach the boundary with open

water and reads quite a bit higher in the open water. We didn't consider data from bands 6-8 (0.7 um to 1.05 um) as they all exhibited very poor results. Here channels 1-4 (0.4 um to 0.6 um) linearly increase going from the oil spill edge to its center. This increase is greatest for channel 5 (0.6 um) occurring much closer to the center of the oil feature than was found for the other channels as shown in Figure 15.

### **3.6 Fusion between SAR and Optical Imagery**

The most important information that we can extract from these optical images is a comparison between the use of optical imagery and SAR data. The backscatter trends, found using TSX data, from the center of the oil spill area towards the border, are less linear than those found using WV2. In fact we can notice more samples that show smaller values of backscatter in the center of the subset. Instead we found the same increase when starting with the water pixels using TSX data. The results found using TerraSAR-X show that the values of backscatter change according to the assumed thickness of the oil spill are indeed smaller near the center of the oil and larger near the border. Also we found that the trends of the spatial profiles from TSX data are similar to the trends found using WV2 data and there are only small differences in the slopes of these trends.

## **4. Discussion and Conclusions**

Analysis of airborne and satellite data has demonstrated sensor capabilities for oil spill detection and characterization. The Ball Aerospace airborne suite provided a unique measurement of thermal and UV imagery on the same platform. Satellite imagery was

used to further characterize the extent and properties of the spill. It is the combination of sensors from airborne, satellite, and shipborne systems that provides the needed reconnaissance for oil spill mitigation.

Additional scientific analysis included data fusion between Optical and SAR satellite imagery for this oil spill. Multi-frequency SAR images were compared with SAR results using X band (TerraSAR-X and COSMO-SkyMed) with those obtained using C band SAR (ENVISAT), of coincident areas and times. Multi-polarization COSMO-SkyMed SAR data results were compared using VV polarization and HH polarization for the same areas and same days. Using multi-sensor data we compared SAR and optical results, of the same areas for the same days. Analyzing all the results obtained in this research we notice that SAR intensity imagery is optimal for oil spill detection. Oil appears darker than the background because oil slicks dampen the capillary waves (wavelength of a few cm) on the ocean surface and reduce the radar backscatter coefficient. Synthetic Aperture Radar has been shown, also in this work, useful and efficient in identifying and quantifying oil spills due to its sensitivity to changes in the sea surface roughness and its ability to observe oceans at night and under cloudy weather conditions.

While it is true that even the satellite SAR sensors may have difficulties in discriminating between oil slicks and competing backscatter changes due to biogenic slicks, very low winds and rain effects, this study of known slicks on the Gulf of Mexico confirms the ability of SAR and optical sensors to both detect and map oil spills. Optical sensors also suffer from the need for atmospheric correction, which was not done in this study. These

are all conditions that need to be taken into account in any future remote sensing study of oil spills.

From the comparison of multi-polarization COSMO-SkyMed SAR data we found that all the values of backscatter, both for the oil and those for the water, are smaller using the VV polarization for all the sites analyzed. We can conclude that the oil spill analysis and detection is more useful and better using the VV polarization instead of HH due to the higher contrast available. We noticed that the values of the standard deviation using VV polarization are larger ( $10^{-3}$  dB) than those obtained using HH polarization ( $10^{-5}$  dB).

These results are consistent with radar theory. From theory, VV polarization gives higher radar backscatter from the sea surface than HH polarization because of the large dielectric constant of the ocean surface. Thus, VV polarized radars will provide more contrast, around 6 dB, (better signal-to-background ratio) when oil is floating on the sea surface. VV is therefore the preferred polarization for detecting oil spill pollution at sea.



## **Acknowledgments**

The authors would like to thank Ray Demara and Shelley Petroy from Ball Aerospace who supported these measurements. Thanks to Dan Soo for the GLIMMER data analysis and Derek Sabatke and Jerod Baker who collected airborne measurements for Ball. We would like to acknowledge DLR and the TerraSAR-X program for providing SAR data over the Gulf of Mexico during the oil spill. We would also like to acknowledge the Italian Space Agency (SAI) for the COSMOSkyMed SAR data provided through Tor Vergata University. We also thank the European Space Agency (ESA) for the Envisat ASAR data (also provided through Tor Vergata Univ) used in this study. We are also grateful to DigitalGlobe Inc. for providing us with the WorldView-2 optical images of the oil spill.

## Reference List

Fingas, M.F., and C. Brown. "Review of Oil Spill Remote Sensing." *Spillcon 2000*, Darwin, Australia, August 16, 2000.

Gade, M., W. Alpers, H. Hühnerfuss, V. Wismann, and P. Lange, "On the reduction of the radar backscatter by oceanic surface films: Scatterometer measurements and their theoretical interpretation," *Int. J. Remote Sens.*, vol. 66, no. 1, pp. 52–70, Oct. 1998.

Hu, C., F. E. Müller-Krager, C. J. Taylor, D. Myhre, B. Murch, A. L.

Odriozola, et al., "MODIS detects oil spills in Lake Maracaibo, Venezuela," *EOS, Trans., American Geophysical Union*, vol. 84(33), pp. 313-319, 2003.

Jha, M.N., J. Levy, Y. Gao. "Advances in Remote Sensing for Oil Spill Disaster Management: State-of-the-Art Sensors Technology for Oil Spill Surveillance." *Sensors*. 8, 236-255, 2008: ISSN 1424-8220.

Osterman, David P, R. Philbrick, W. Good, L. Schneider, E. Saiki, A. Clark, P. Johnson, R. To, T. Lin, "Test results from an imager for scenes with high dynamic range and low light levels." *Proceedings of SPIE*, Vol. 7807-06, August, 2010.

Tseng, Y. W. and L.S. Chiu. "AVHRR observations of Persian Gulf oil spills", *Int. Geoscience and Remote Sensing Symp. (IGARSS)*, Pasadena, USA, 1994, vol.2, pp. 779-782.

Wismann, V., R. Theis, W. Alpers, and H. Hühnerfuss, "The damping of short gravity capillary waves by experimental sea slicks measured by a multifrequency microwave scatterometer," in Proc. OCEAN, vol. II, Victoria, Canada, 1993, pp. 342–347.

**Table Captions:**

Table 1: Ball Aerospace airborne instrument parameters

## **Figure Captions:**

Figure 1: Ball Instruments installed on plane (top down view on runway) – GLIMMER at top left, BESST at top right, LLI below

Figure 2: Ball Experimental Sea Surface Temperature (BESST) Radiometer

Figure 3: The 8 bands of WorldView-2

Figure 4: Flight data showing thermal IR imagery in clear water (a) and with thick oil (b) – Latitude and longitude on the axes with temperature in degrees Celsius. Location of Deepwater Horizon Platform also shown for reference.

Figure 5 (a,b): Flight paths and composite oil location determined from ERMA compilation website on July 9<sup>th</sup> (left, a) and July 10<sup>th</sup> (right, b). Oil only detected on July 9<sup>th</sup> consistent with satellite composite.

Figure 6: GLIMMER 2 nm band sampling from 350-400 nm showing varying scene intensity with wavelength over oil

Figure 7: LLI geolocated context image of oil (bright) on water background – latitude and longitude on the axes with flight path and image location shown

Figure 8: Total Surface Oil between May and July, 2010

Figure 9: Terra-SAR-X image of July 5, 2010

Figure 10: TSX Error Plot Mean Object and Background July 5, 2010

Figure 11: Altimetry currents for July 6, 2010 in the Gulf of Mexico

Figure 12: COSMO-SkyMed April 25, 2010

Figure 13: July 5, 2010 TerraSAR-X (top) and ENVISAT ASAR (bottom); the different rectangles indicate common locations on each image

Figure 14: Spectral profiles (microns) for WorldView 2 during the Deepwater Horizon Spill

Figure 15: Spatial profile from the edge of the oil spill to the center

**Tables:**

Table 1:

<b>Specification</b>	<b>BESST</b>	<b>GLIMMER</b>	<b>LLI</b>
<b>Wavelength range</b>	<b>8-13 um</b>	<b>0.35-0.70 um</b>	<b>0.46-0.86 um</b>
<b>FOV</b>	<b>13 degrees</b>	<b>16 degrees</b>	<b>28 degrees</b>
<b>Swath Width @ 1070 m altitude MSL</b>	<b>250 m</b>	<b>300 m</b>	<b>570 m</b>
<b>Surface resolution</b>	<b>1.0 m</b>	<b>0.7 m</b>	<b>0.3 m</b>

**Figures:**

Figure 1:





Figure 2:

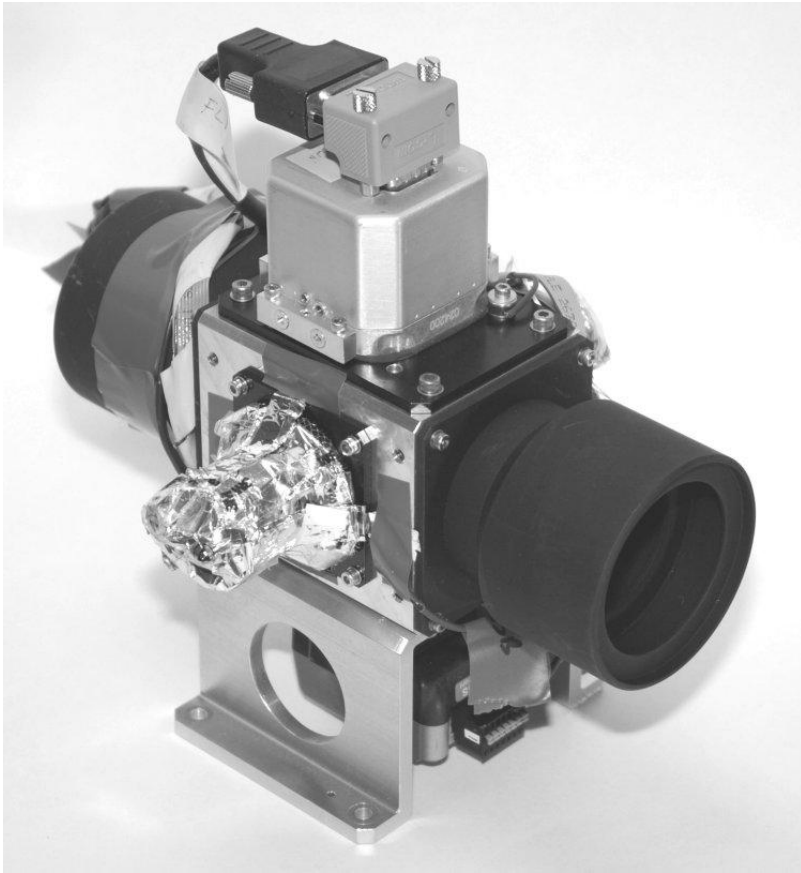


Figure 3:

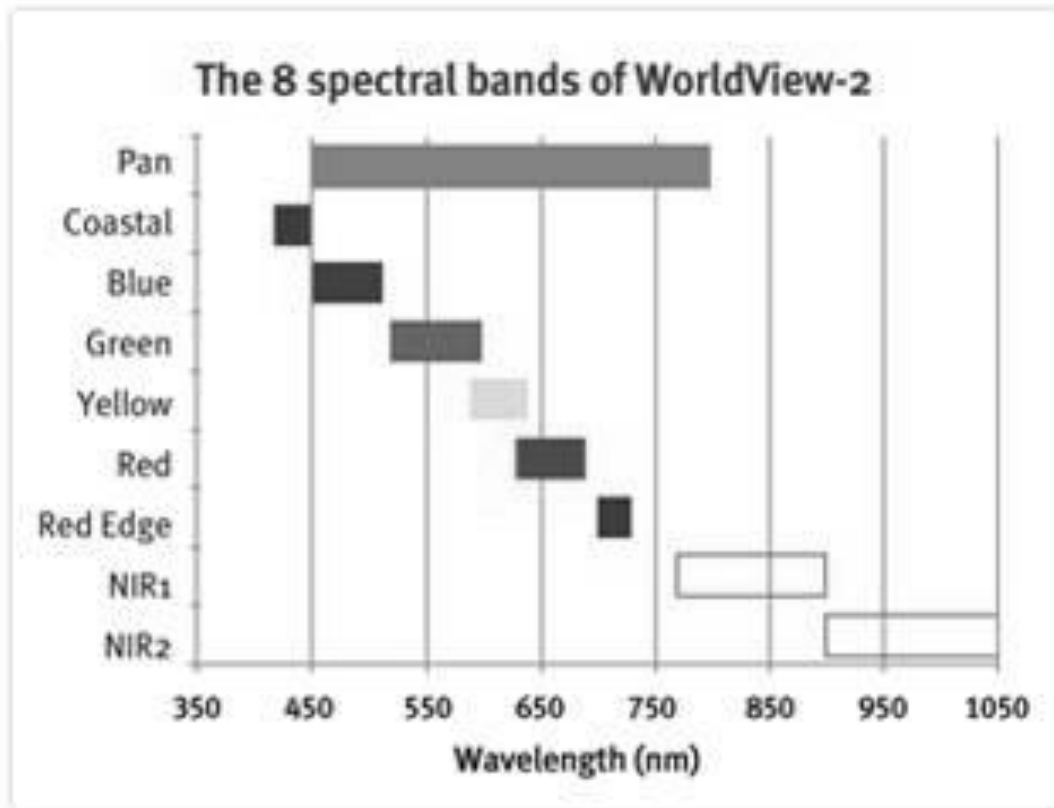


Figure 4 (a,b):

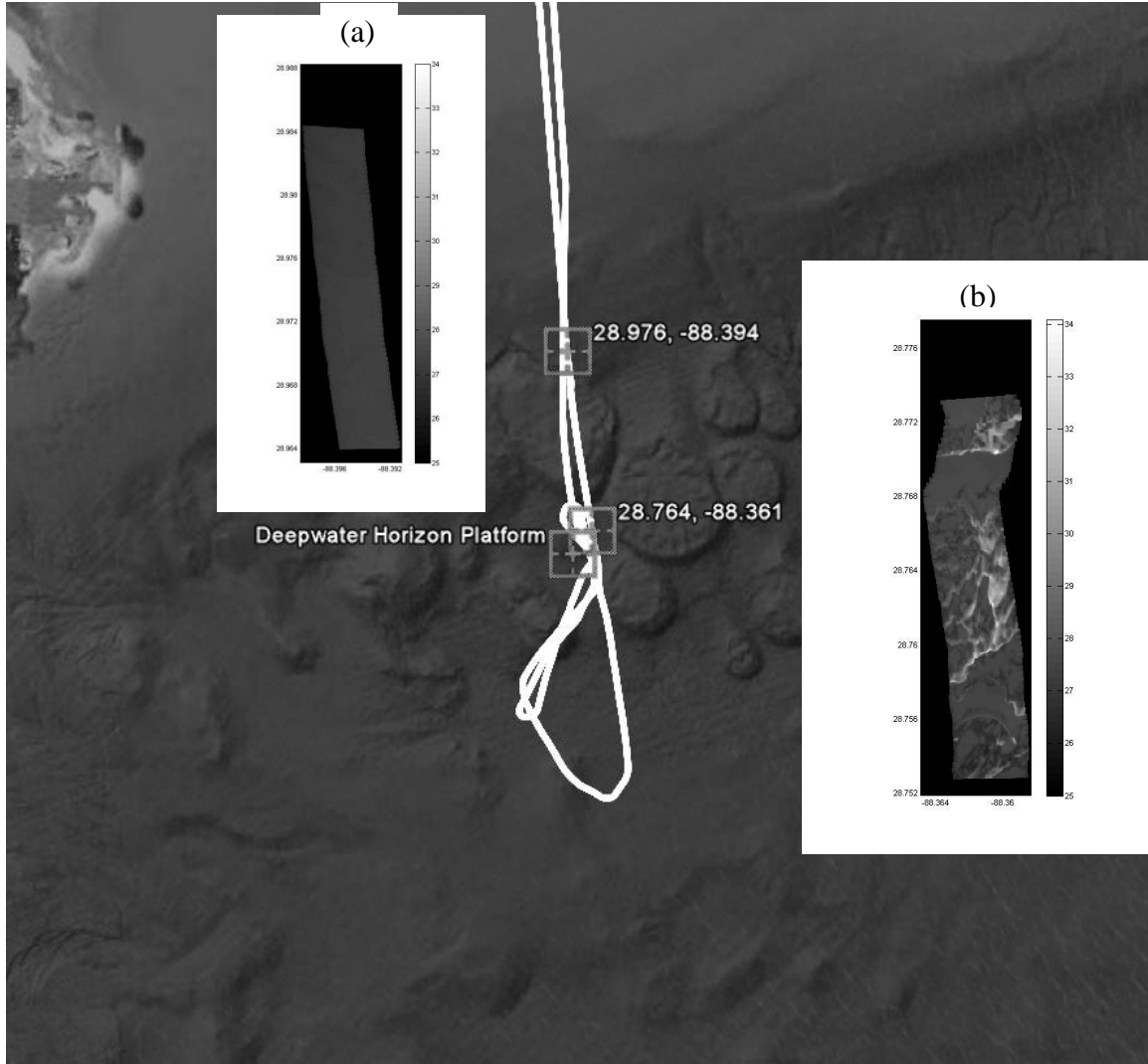


Figure 5 (a,b)

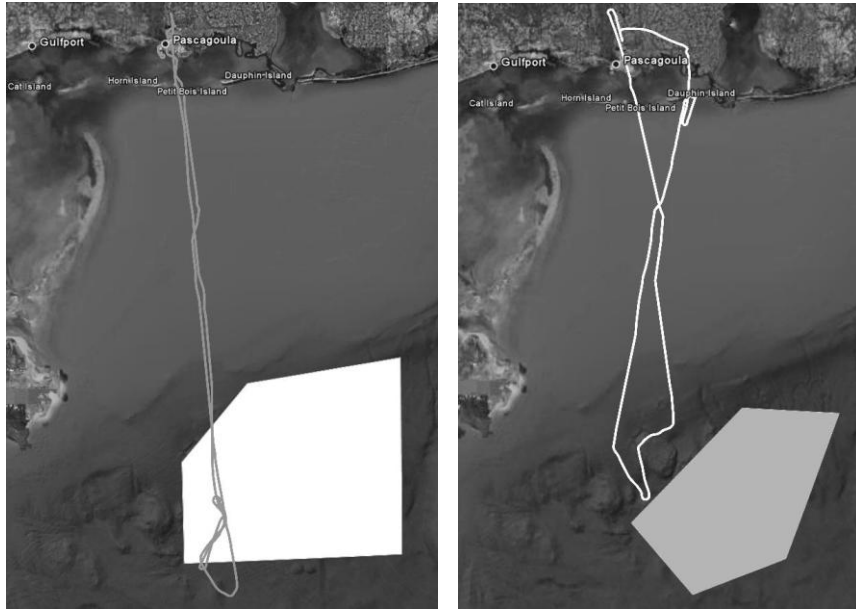


Figure 6:

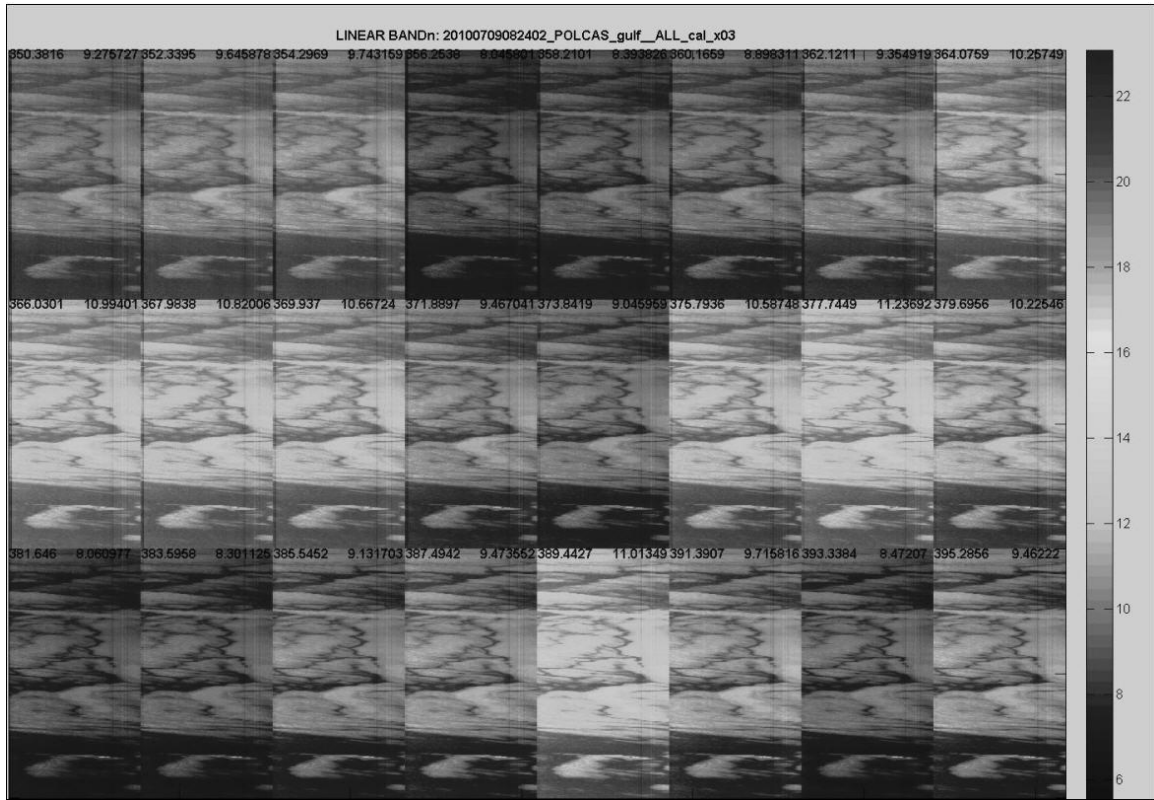


Figure 7:

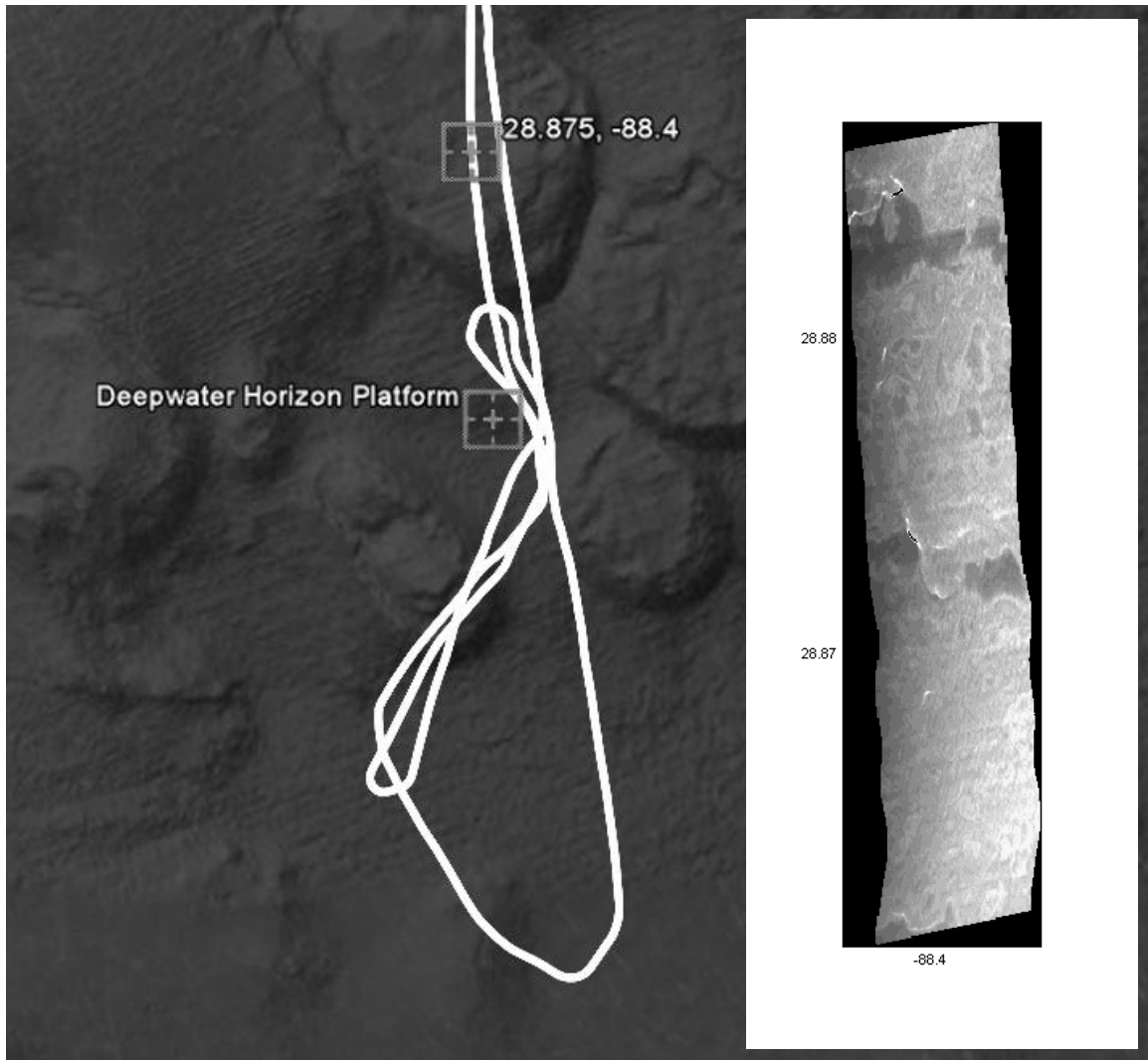


Figure 8:

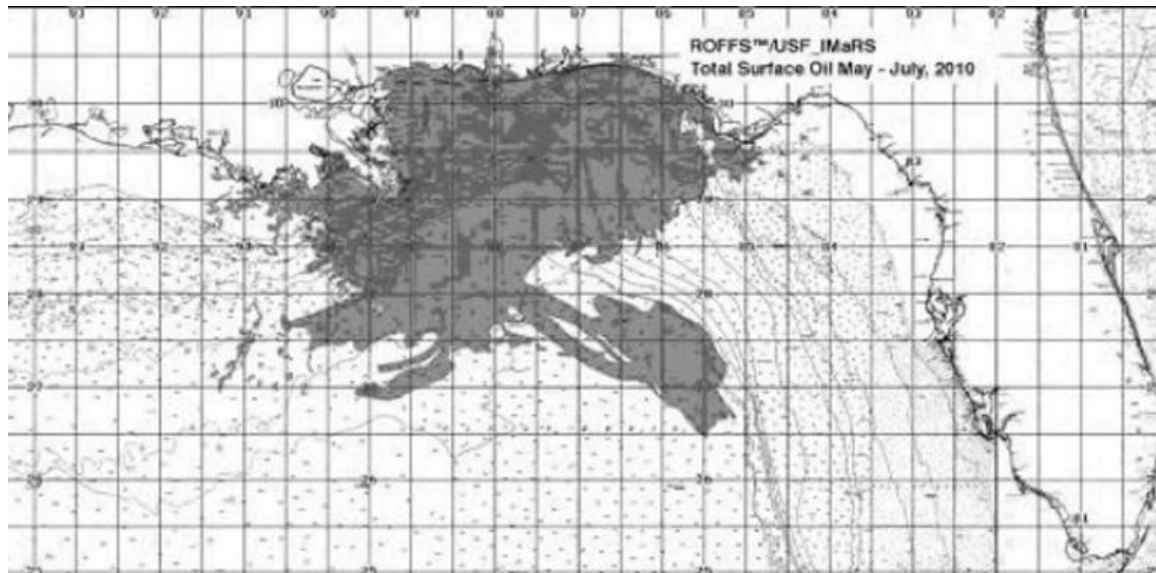


Figure 9:





Figure 10:

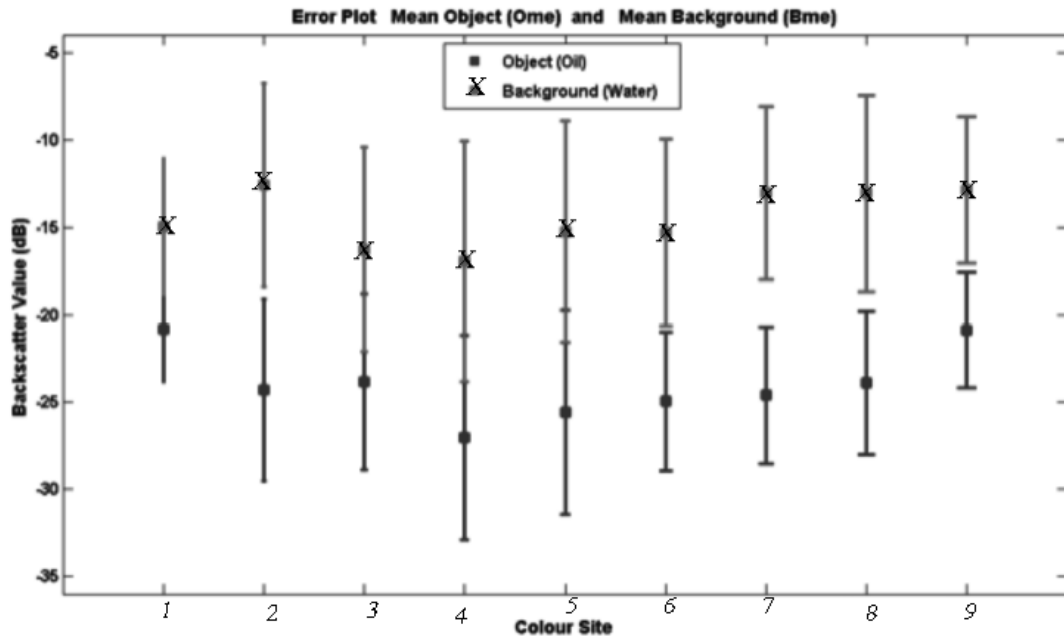


Figure 11:

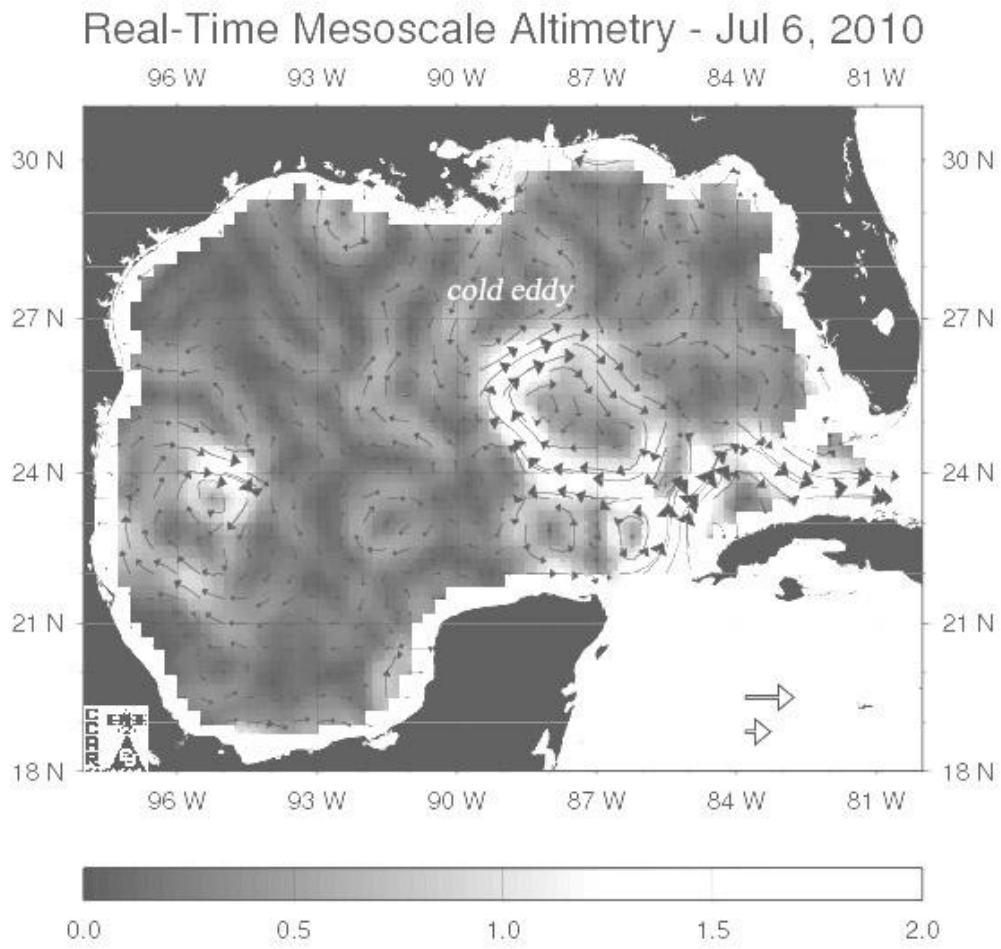


Figure 12:

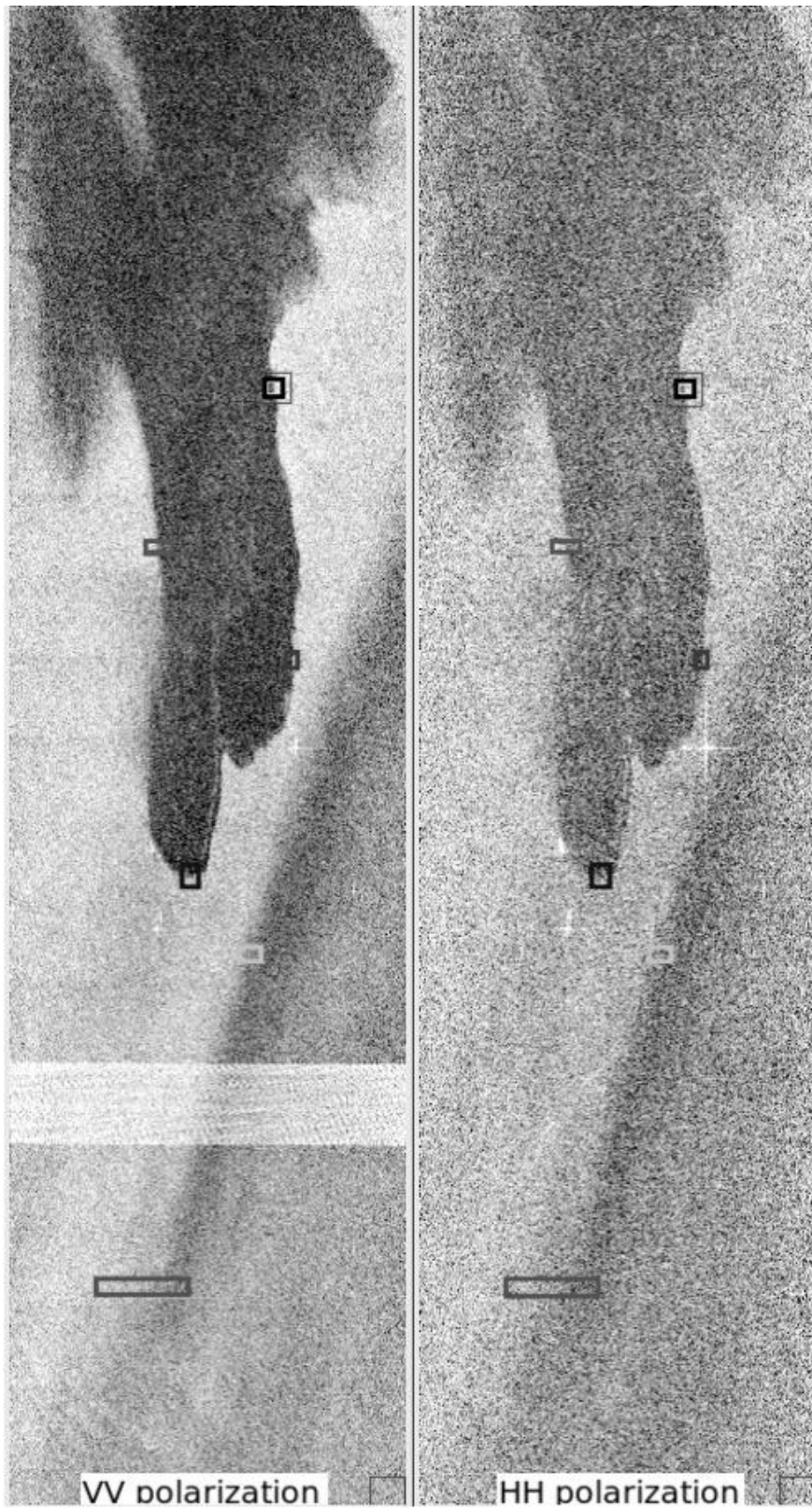


Figure 13:



July 5, 2010  
ENVISAT ASAR Part 1

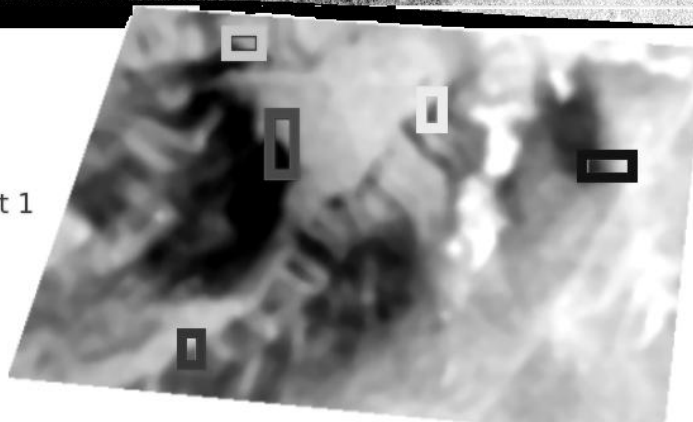


Figure 14:

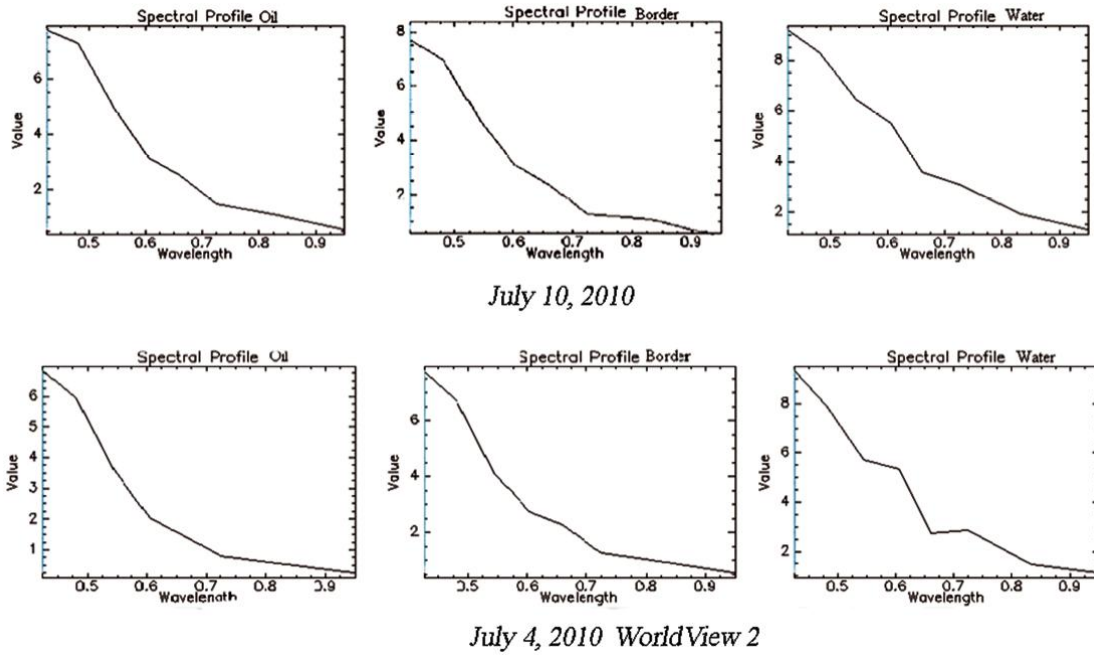


Figure 15:

